PCCP
Physical Chemistry Chemical Physics

Accepted Manuscript

This article can be cited before page numbers have been issued, to do this please use: Y. Lomachuk, D. Maltsev, N. S. Mosyagin, L. Skripnikov, R. V. Bogdanov and A. V. Titov, *Phys. Chem. Chem. Phys.*, 2020, DOI: 10.1039/D0CP02277B.

View Article Online
DOI: 10.1039/D0CP02277B

PCCP

ARTICLE TYPE

Cite this: DOI: 00.0000/xxxxxxxxxx

Compound-tunable embedding potential: Which oxidation state of uranium and thorium as point defects in xenotime is favorable?

Yuriy V. Lomachuk,*[a] Daniil A. Maltsev,[a] Nikolai S. Mosyagin,[a] Leonid V. Skripnikov,[a,b], Roman V. Bogdanov,[a,b] Anatoly V. Titov.[a,‡]

Received Date
Accepted Date

DOI: 00.0000/xxxxxxxxxx

Modern strategies for safe handling of high level waste (HLW) and their long-term disposal in deep geological formations include the immobilization of radionuclides in the form of mineral-like matrices. The most promising matrices for immobilization of actinides are ceramic forms of waste based on phosphate minerals such as monazite, xenotime, cheralite. However, the mechanism of substitution of lanthanides and Y by actinides in phosphate minerals is not entirely clear. We formulate a theoretical model, *compound-tunable embedding potential* (CTEP), that allows one to predict properties of such crystals with point defects. Reliability of the model is validated by a good agreement of calculated geometry parameters with available experimental data. Substitution of Y in the xenotime crystal by Th and U is studied by relativistic DFT in the framework of the CTEP method, based on constructing the embedding potential as linear combination of short-range "electron-free" spherical "tunable" pseudopotentials. It is shown on the basis of proposed model that oxidation state $+3$ is energetically more profitable than $+4$ not only for thorium but also for uranium as solitary point defects. This atypical oxidation state of U in mineral is discussed.

Introduction

Natural orthophosphates of yttrium and rare earth elements (minerals like xenotime YPO_4 and monazite $CePO_4$) are characterized by high chemical and radiation resistance [1] and are considered as natural analogues of matrices for immobilization of actinides [2–4].

Methods for the high-temperature synthesis of ceramics based on these orthophosphates have been developed in detail, conditions for the stabilization of actinides in the tri- and/or tetravalent states have been found [5–7] (higher degrees of oxidation of actinides are not formed in this case [8]). It is assumed that the resulting composites will be buried in deep geological formations for a period of at least 10,000 years [9]. However, understanding the immobilization properties of such matrices at the atomic level can be reliably achieved only on the basis of quantum-chemical modeling the electronic structure of the considered actinide-containing materials.

Accurate calculation of actinide-containing molecules for wide variety of properties is yet problematic to-date because of their multireference character, although density functional theory (DFT) and wave-function theory (WFT) based studies for the ground-state electronic structures and for compounds of actinides in their highest oxidation states can be quite reliable (see review [10], more recent studies [11–13] and references therein). Note, however, that recent developments in coupled-cluster theory [14,15] are quite optimistic to believe in a good prospect of the WFT based applications to actinide-containing compounds of medium size (about a dozen(s) of atoms) in near future. In turn, in electronic structure calculations of solids one should study periodic structures that dramaticaly complicate applicability of WFT based approaches [16]. However, for relatively low concentration of actinides in solids it is reasonable to utilize cluster models to study some fragments of these minerals in the WFT framework. In this case, the calculation is carried out only for relatively small region that includes an impurity atom and its environment. The remaining part of the crystal is modeled by an embedding potential, to account for influence of environment on the selected fragment of the crystal. Such a modeling scheme is known as the embedded cluster method [17]. Mention here hybrid methods of molecular modeling (e.g., see [18,19]) which are also popular to study physical-chemical properties of actinide-containing substructures.

While good incorporation of Th into monazite is naturally justified by approximately the same ionic radii of Ce and Th atoms [20] and similarity of their electronic structure, there are no such analogy between Y and U (Th) atoms for the case of xenotime. Therefore, one needs in a more detailed consideration based on theoret-

[a] Petersburg Nuclear Physics Institute named by B.P. Konstantinov of National Research Center "Kurchatov Institute" (NRC "Kurchatov Institute" – PNPI), 188300, mkr. Orlova roscha, 1., Gatchina, Leningradskaya oblast, Russian Federation .
[b] Saint Petersburg State University, 7/9 Universitetskaya nab., 199034, St. Petersburg, Russia
* E-mail: Lomachuk_YV@pnpi.nrcki.ru, jeral2007@gmail.com
‡ E-mail: Titov_AV@pnpi.nrcki.ru

View Article Online
DOI: 10.1039/D0CP02277B

ical electronic structure modeling of xenotime with the impurity actinide atoms.

The grounds of new, combined approach based on the relativistic study of materials and their fragments with inclusion of impurity atoms (which can be *f* and heavy *d* elements) is developed by us on the basis of the *compound-tunable embedding potential* (CTEP) method [21,22] (see next section for details). Electronic structure calculations with CTEP of the point defects containing uranium and thorium made it possible to determine a number of their characteristics. One of the most interesting questions is that about the energetically preferred oxidation state of thorium and uranium in xenotime. According to Goldschmidt's long-standing paper [23] it should be +4, not +3. More recently, Vance *et al.* wrote in ref. [5] "Thus overall the results for U were broadly similar to those for Np and Pu, except that only tetravalent U was observed" and "U^{+3} should also be able to be incorporated in principle but the necessary conditions would likely be so reducing that the xenotime and monazite structures would be destabilized by the reduction of phosphate to elemental P." Thus, the question about the +3 oxidation state of U in xenotime is yet open and one of goals of this research is to discuss this problem from theoretical point of view.

Our cluster model is given in section "Computational details", results of calculation are considered in "Results", and discussion about absence of experimental data with trivalent U is given in "Discussion".

1 Compound-tunable embedding potential theory

In the framework of CTEP version of the embedding potential theory, the following procedure for calculating the electronic structure of a crystal fragment which can include a point defect is implemented:

(1) High-level periodic DFT calculation of a crystal without point defects.

(2) Cutting a fragment out of a crystal with a central metal atom/ion (which can be further replaced by a vacancy, impurity atom, etc.) and the ligands attached to it. Thus, the first coordination sphere consists of a small number of atoms that is usually not more than 12 (as in the case of dense packing). This structure will be referred further as the "main cluster".

(3) For the main cluster one can first choose a *nearest cationic environment*, NCE, from the lattice atoms (second coordination sphere, etc.) and then, a *nearest anionic environment*, NAE, including a set of all anions which are nearest to the NCE atoms except those of the main cluster. The main cluster together with the nearest environment, i.e. main cluster + NCE + NAE (or main cluster + CTEP), will be referred as the *extended cluster*, or just a cluster.

The NCE is described by means of pseudopotentials (PP) generated for cations $A_n^{X_n+}$, where "+" stands for a cationic state of atom A_n corresponding to the o*X*idation state (*n*umber) $+X_n$ (X_n runs over natural numbers), such that all the electrons of the cations are treated within the PPs as core ones (and below designated as 0ve-PPs or "big-core" PPs). Thoroughly, 0ve-PP/$A_n^{X_n+}$ generated for a given AiC effective state is written as

$$\begin{aligned}\mathbf{U}_n^{0\mathrm{ve/AiC}} = \quad & +X_n/r + V_L^n(r) + \\ & \textstyle\sum_l^{l_{\max}} [V_l^n(r) - V_L^n(r)] \sum_{m=-l}^{l} |l,m\rangle\langle l,m| \ ,\end{aligned} \tag{1}$$

where standard expression for the spin-averaged semilocal (radially-local) PP operator is used (e.g., see [28] and references; here *l* and *m* mean angular momentum and its projection for one-electron states; $L>l_{\max}$, where $l_{\max}$ is highest angular momentum for electrons in the atomic core). Emphasize that the 0ve-PPs can be considered as "free-electron" PPs assuming that we do not attach more electrons to the extended cluster additionally to those already involved in the main cluster in accord to the oxidation numbers of the main-cluster atoms. In practice, the known schemes of population analysis on atom A_n will not give exact zeros for occupancies of its valence orbitals even on alkali metals, and the degree of covalence for the ionic bonding should be taken into account at the big-core PP generation stage for NCE atoms in a compound to take account of the core relaxation.

Each NCE atom is described by the semi-local PP and fractional point effective charge. "Tuning" the 0ve-PPs for environmental cations is carried out self-consistently in the periodic DFT calculations of pure crystal to minimize displacement forces on atoms A_n and others in the unit cell at the optimized DFT geometry of the crystal obtained at step (1). The $\mathbf{U}_n^{0\mathrm{ve/AiC}}$ PPs are constructed by us basically following the scheme for the "self-consistent" PP version proposed in [28,29] to fit the AiC effective state of the $A_n^{X_n+}$ cations in the crystal (details of the CTEP generation procedure will be described elsewhere).

The general formula for the CTEP is

$$\begin{aligned}\mathbf{U}_{\mathrm{CTEP}}(\vec{r}) = \quad & \textstyle\sum_{n\in NCE} \left(\mathbf{U}_n^{0\mathrm{ve/AiC}}(\vec{r}-\vec{r_n}) + \frac{q_n}{|\vec{r}-\vec{r_n}|} \right) + \\ & \textstyle\sum_{a\in NAE} \left(\frac{q_a}{|\vec{r}-\vec{r_a}|} \right) \ ,\end{aligned} \tag{2}$$

where $\mathbf{U}_n^{0\mathrm{ve/AiC}}$ are "electron-free" PPs from Eq.(1) for corresponing NCE cations $A_n^{X_n+}$ which are "tuned" to fit the effective states of atoms (cations) in a compound, AiC, according to the chosen main cluster in the crystal under consideration. The tuning partial charges, negative, $q_n=-|q_n|$, for cations and positive, $q_a=+|q_a|$, for anions reflect the "polarization" of those electronic shells which are treated implicitly for the NCE and NAE atoms in the compound and simulate in our current CTEP model the electric field of environment acting on the main cluster.

Both the NAE and NCE charges located at the lattice sites are optimized when constructing the CTEP to reproduce the spatial structure of the main cluster as a fragment from the periodic study (at step 1) in the molecular-type calculation of the extended cluster with only point symmetry of the crystal fragment taken into account. Our current charge optimization criterion is minimization of sum of squares of forces on atoms from the main cluster, with the constraint that the total charge of the extended cluster is fixed to zero (see next section). Note, that relaxation of electronic structure in both main cluster and nearest environment regions is taken into account within CTEP when one considers processes and point defects localized on the main cluster despite the coordinates of the environmental atoms are not changed.

View Article Online
DOI: 10.1039/D0CP02277B

The key feature of the CTEP approach is its applicability to fragments of a crystal of minimal size that can include only nearest environment of a central atom. Note that calculation of a crystal fragment of small size (including up to $\sim 6 \div 12$ atoms, with a central f (or d) element and its first anionic coordination sphere) using CTEP and combining[27,30] advanced two-component (relativistic) versions of density functional[31] and coupled-cluster (see[14,32,33] and refs.) theories can be done in practice. Furthermore, one can perform relativistic calculation of a larger cluster with the chosen DFT functional with actinide impurities and vacancies to take relaxation of its neighbors into account. The relativistic coupled-cluster (RCC) corrections to the DFT calculation of the cluster can also be done (see pilot combined study in[27]).

2 Computational details

The DFT method with hybrid PBE0[34] functional implemented in the CRYSTAL code[35] was used to carry out electronic structure calculations of the xenotime crystal. This code allows one to use the same PBE0 functional and basis sets as those in the cluster model calculations, both one- and two-component, which are discussed below. Thus, one can directly juxtapose results of these calculations.

The cluster model calculations were carried out with using the two-component DFT code[36]. To avoid significant basis set superposition error (BSSE) arising from presence of diffuse type orbitals at simulating the crystal structure, we use the relatively small basis sets for such calculations. It is also important to note, that using the same basis sets, atomic PPs and DFT-functional for the periodic crystal and cluster model calculations allows one to estimate reliably the errors arising from using the embedded cluster model simulating the crystal fragment.

The PPs for yttrium developed by our group[28,37] was applied to exclude core shells from calculation such that only 11 outermost yttrium electrons are treated explicitly. The uncontracted basis set (5s4p3d)[37] was used for these electrons.

The oxygen and phosphorus atoms are treated at all-electron level, basis sets for them are taken from[38].

We consider the following cluster model of xenotime crystal to perform calculations of properties of Y, Th, U atoms in xenotime: the structural formula of our cluster is Y-$(PO_4)_6$-Y'_{22}-O'_{104}. The main cluster, Y-$(PO_4)_6$, consists of the central yttrium (substituted later by uranium or thorium) atom and surrounding six orthophosphate groups PO_4 (see Figure 1). For the main-cluster atoms, the same PP and basis sets for Y, P, O atoms were used as for the periodic structure calculations. To reproduce the electronic structure of a fragment in a crystal (in particular, saturate chemical bonds properly) we need first reproduce the oxidation states of the atoms inside the fragment. For the main cluster we have +3 for oxidation state of Y and -3 for each PO_4 group. Thus, 15 additional electrons should be added to the main cluster, which, in turn, should be compensated by the charge of environment (see below).

The cationic layer of the cluster model, Y'_{22}, consists of 22 yttrium pseudoatoms, which are modeled with using particular kind of the "electron free" PP[21], with respect to the Y^{+3} oxidation state ("electron free" PP means here that we do not introduce

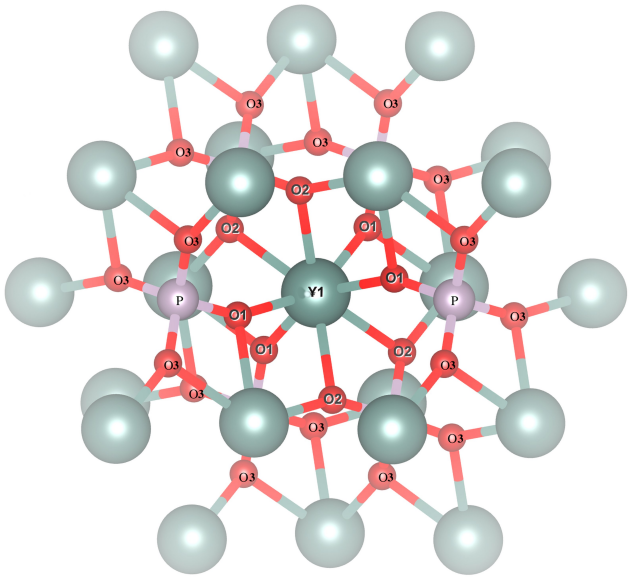

Fig. 1 Xenotime YPO_4 cluster model. The cluster model structural formula is Y–$(PO_4)_6$–Y'_{22}–O'_{104}. The anionic layer, O'_{104}, is not presented on this figure due to the limited space. The cationic layer pseudoatoms, Y'_{22}, are displayed as shaded spheres. The central yttrium atom Y1 and P atoms of main cluster are denoted by corresponding labels. There are three types of O atoms in the main cluster area – oxygen atoms of these types labeled as O1, O2 and O3. The Y–O bond lengths between central Y1 atom and oxygen atoms of types O1 and O2 differ from each other. The atoms labeled as O1 belong to the one orthophosphate group in the main cluster area, while atoms of the second type belong to two adjacent orthophosphate groups. The O3 atoms of the main cluster are not chemically bonded to the central yttrium atom.

View Article Online
DOI: 10.1039/D0CP02277B

additional electrons to the extended cluster under consideration compared to the main one). The basis sets used for these atoms were taken here the same as for the central yttrium atom.

The anionic layer, O'$_{104}$, consists of the 104 oxygen-site negative point charges without addition of electrons to the cluster as well. The net charge of 15 additional electrons to the main cluster is completely compensated by the corresponding fractional charges on yttrium (cationic) and oxygen (anionic) sites of the environmental layers. In our approach, the additional charges on these yttrium pseudoatoms as well as oxygen-site negative point charges of the anion layer are considered as adjustable parameters of the CTEP for xenotime.

In the present work, values of these charges were obtained by minimizing root mean square (RMS) force $|f|$ acting on the atoms of the main cluster. This value is calculated as

$$|f| = \sqrt{\sum_{i=1}^{N_{at}} \left(\nabla_i E\right)^2 / N_{at}}, \quad (3)$$

where E is the evaluated total energy of the cluster, N_{at} – number of atoms in the main cluster ($N_{at} = 31$ for the xenotime cluster model), and ∇_i is the gradient operator with respect to coordinates of nucleus of i-th atom.

The basis sets and PPs developed by our group[37] were used for calculations of xenotime with the U and Th point defect substitutes of Y.

3 Results

3.1 Periodic structure calculation results

According to the experimental data[39] the crystal system of the xenotime YPO_4 is tetragonal (lattice parameters $a = b \neq c$, $\alpha = \beta = \gamma = 90^\circ$). The space group is $I4_1/amd$ and there are 3 non-equivalent atoms Y, P, O in the unit cell.

The lattice parameters as well as positions of the atomic nuclei within the unit cell of the crystal were optimized to achieve minimum of the total energy of the system. The results of calculation are given in Table 1.

The computational errors include those of the approximate nature of exchange-correlation PBE0 functional, the basis set incompleteness (that is rather dramatic in practice for periodic and many-atomic systems) and the PP errors. At the CTEP generation stage (see the following section) we use the same DFT functional, basis sets and PPs as in the periodic study calculation, however, in subsequent small-cluster studies with CTEP, one can seriously increase the basis set size and use small-core PPs to reduce the corresponding errors. As a result, the PBE0 errors are expected to be leading ones in the final DFT studies with CTEPs and can be estimated by comparing theoretical results with experimental data. Discussion about typical DFT errors (including PBE0 functional) is given in paper[40] and our PBE0 errors, which are about 0.04 Å for lattice parameters and Y–O and P–O bond lengths are in line with those, that given in Ref.[40].

Table 1 Results of the calculations of Y-$(PO_4)_6$-Y'$_{22}$-O'$_{104}$ cluster model and xenotime crystal

	expt. data	crystal calculations	cluster model calculations
$a = b$, Å[a]	6.89	6.93	–
c, Å[a]	6.03	6.06	–
Q_Y, a. u.[b]			2.6 ± 0.1[c]
Q_O, a. u.[b]			-0.4 ± 0.3[c]
$\|f\|$, a.u.[d]			3.6×10^{-4}
Y–O1, Å[e]	2.32	2.32	2.317 ± 0.002
Y–O2, Å[e]	2.38	2.37	2.372 ± 0.004
P–O, Å[e]	1.54	1.57	1.566 ± 0.001

[a] The lattice parameters obtained from the DFT PBE0[34] periodic structure calculations using the CRYSTAL[35] code; the experimental data are taken from[39].
[b] The Q_Y and Q_O are average additional charge values on the Y' pseudoatoms of cluster cation layer Y'$_{22}$ and on the O' pseudoatoms of cluster anion layer, correspondingly. The whole sets of these values were optimized to minimize RMS force acting on the main-cluster atoms, when the atom nuclei positions obtained from the crystal calculations are used.
[c] Standard deviation of the value x calculated on the sets of additional charges of cation layer atoms for $x = Q_Y$ and of anion layer atoms for $x = Q_O$.
[d] RMS force acting on the atoms of the main cluster Y-$(PO_4)_6$. This value is calculated from equation (3).
[e] The P–O, Y–O1 and Y–O2 bond lengths (see Figure 1). In the cluster model calculations column, average values for the atoms of the main cluster are represented. Errors for them are estimated as corresponding standard deviations.

3.2 Calculation of CTEP parameters for cluster studies

The CTEP is generated for the cluster model of the xenotime Y-$(PO_4)_6$-Y'$_{22}$-O'$_{104}$ (see Figure 1) using the calculated periodic structure data. Due to the lower symmetry of the cluster, for which only point group can be taken into account as compared with xenotime crystal, the yttrium pseudoatoms of the cationic layer are not equivalent to each other; the same is true for the oxygen-site negative point charges of the anionic layer. This fact leads to dispersion in values of additional charges on yttrium and oxygen pseudoatoms. To provide estimation of this dispersion we calculate standard deviations ΔQ_Y, ΔQ_O as

$$\Delta Q_X = \sqrt{\frac{1}{N_X} \sum_a (q_a - Q_X)^2}, \; X = Y, O, \quad (4)$$

where the Q_Y, Q_O are the average additional charges on the yttrium and oxygen pseudoatoms, correspondingly, q_a is the additional charge value on the pseudoatom, and we perform summation over all pseudoatoms indicies of the NCE for X=Y, and of the NAE for X=O. The results of charge optimization procedure are listed in Table 1.

Optimal values of charges Q_Y are spread around average value $\langle Q_Y \rangle \approx 2.6 \pm 0.1$, this value is in qualitative agreement with the corresponding formal charge +3. RMS force acting on the main-cluster atoms $|f|$ is of the order of 10^{-4} a. u.

To obtain more illustrative estimate of quality of the described cluster model, positions of the main-cluster atoms were optimized to achieve minimum of the total energy of the system. During this

View Article Online
DOI: 10.1039/D0CP02277B

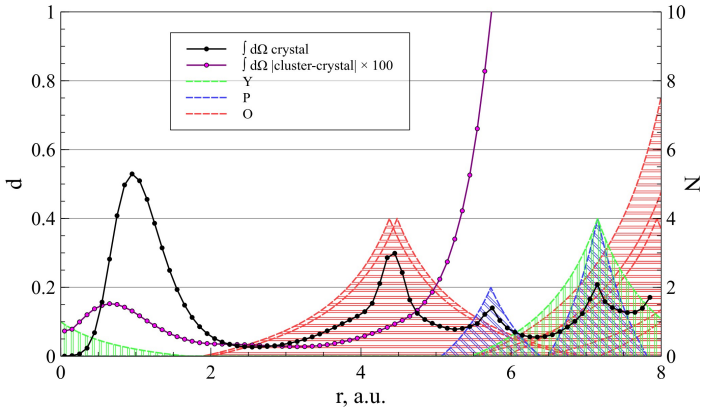

Fig. 2 The radial dependence of electronic density differences for the original (non-substituted) cluster. Solid line corresponds to the integral of absolute difference $d(r)$. Filled peaks at the bottom qualitatively represent the position of the neighbour atoms (color denotes atom type, width at the bottom is equal to crystal radius, and the peak height is proportional to the number (N on the right scale) of atoms at the same distance to the center).

optimization process, positions of pseudoatoms from cationic and anionic environmental layers were considered as fixed together with the values of additional charges. Difference between the optimized cluster and calculated crystal values for the Y–O and P–O bond lengths is of the order of 10^{-3} Å, this value is much less than the difference between the results of crystal calculation and experimental data. Due to the symmetry lowering in cluster model mentioned above, there is a dispersion in values of the optimized Y–O and P–O bonds lengths in the cluster. We present standard deviation of these values in the cluster (calculated by the formula similar to Eq. 4), to show that errors arising from symmetry lowering are of the order 10^{-3}.

To estimate the reproducibility of the electronic properties of the original non-substituted cluster, compared to the solid-state calculations, electronic density cube files were obtained for the periodic crystal study and for the cluster with CTEP. The cube grid was chosen to be the same in both cases with the orthogonal unit vectors of about 0.053 a.u.

As a quantitative criterion we provide the angle-averaged difference between the cluster and crystal electronic densities, calculated by the following formula:

$$d(r) = \frac{1}{4\pi} \oint d\Omega \left| \rho_{cluster}(\vec{r}) - \rho_{crystal}(\vec{r}) \right| ,$$

where the $\vec{r}$ is the radius vector of the point with origin in the central atom nucleus site, the $d\Omega$ is the differential solid angle, and the $d(r)$ represents the absolute magnitude of difference.

This value is plotted at the Figure 2 as the solid line. The bottom curves qualitatively represent the electronic density of atoms from the main cluster. The black curve is the total density, and the difference curve is multiplied by factor of 100.

3.3 Properties of Th and U in xenotime

The effective states of impurity uranium and thorium atoms in xenotime were studied in calculations of the clusters with the above constructed xenotime cluster model and the above generated CTEP, in which the central yttrium atom is substituted by the U or Th atom. For both cases four different types of calculations were carried out, with 15, 14, 13 and 12 additional electrons in the main cluster (that is not neutral in the last three cases in contrast to the extended one at the CTEP generation step). The first two calculations are corresponding to the cases of X^{+3} and X^{+4} (X= Th, U) oxidation states of the appropriate defects in xenotime. While the clusters with 13 and 12 additional electrons for central uranium atom case correspond to the cases of the U^{+5} and U^{+6} oxidation states, analogous clusters with central thorium atom correspond to the Th^{+4} oxidation state and ionized neighboring PO_4 groups (see Table 2). Positions of atoms in the main cluster with actinides were optimized to minimize its total energy. Results of these calculations are listed in Table 2.

To determine if the cases of 14, 13 and 12 additional electrons in the main cluster correspond to the X^{+4}, X^{+5}, X^{+6} oxidation states of the central atom X (Th or U), or not, Bader's charge analysis[42] were performed for all the studied clusters with using BADER code[41]. The evaluated Bader net charges show that the case of 14 additional electrons corresponds to the X^{+4} substitute in the main cluster (X=Th, U), whereas 13 and 12 additional electrons in the main cluster correspond to X^{+5} and X^{+6} substitute only for case of X=U.

The evaluated Y–O and P–O bond lengths show that the defects of Th and U being in the +3 oxidation state deform the crystal cell much more than those in the +4 oxidation state. This can be explained by the fact, that despite the trivalent Th and U have the same formal charge as Y^{+3} in YPO_4, the tetravalent ones have significantly smaller ionic radii[20], which are comparable with that of Y^{+3}.

Let us consider spin density $|\vec{S}(\vec{r})| = \sqrt{S_x^2(\vec{r}) + S_y^2(\vec{r}) + S_z^2(\vec{r})}$ appearing around Th and U upon introducing the impurity atoms into the crystal. It formed mainly by electrons on the open d and f shells of these atoms. Since radial parts of electronic wavefunctions of these shells are different, it is possible to estimate occupations of these shells from the specific form of the spin density distribution.

The spin density distributions in the clusters with impurity uranium atom are presented on Figure 3. It follows from the data that the numbers of electrons on the open $5f$-shell of U correlate with the numbers of additional electrons in the cluster. Note that one cannot extract the corresponding information from the conventional population or Bader analyses since they take into account contribution of the f-orbitals to U-O bonding states that largely compensate (more than on 50% the different numbers of additional electrons.

The spin density distributions in the clusters with impurity thorium atom are presented on Figure 4. From the data one can conclude that there is one electron on the thorium valence shells in the cluster with 15 additional electrons (this case corresponds to the $6d^x7s^{1-x}$ configuration of the free Th^{3+} ion); in the case of

View Article Online
DOI: 10.1039/D0CP02277B

Table 2 Properties of thorium and uranium impurity atoms in xenotime[a]

	YPO_4 [a]	TPO	$(TPO)^{+1}$	$(TPO)^{+2}$	$(TPO)^{+3}$	UPO	$(UPO)^{+1}$	$(UPO)^{+2}$	$(UPO)^{+3}$
Q_X, bader charge, a. u.[b]		2.4	3.0	3.0	3.0	2.3	2.8	3.0	3.2
$\langle\lvert\vec{S}\rvert\rangle$, a. u.[c]		1.1	0.0	1.2	2.4	2.8	1.9	1.1	0.0
P - O, Å[d]	1.56	1.56	1.54 – 1.58	1.54 – 1.58	1.54 – 1.56	1.56	1.55 – 1.59	1.54 – 1.62	1.51 – 1.67
X - O1, Å[d]	2.32	2.42	2.32	2.32	2.32	2.40	2.29	2.15 – 2.34	2.06 – 2.10
X - O2, Å	2.37	2.47	2.40	2.37	2.4	2.45	2.37	2.15 – 2.34	2.25 – 2.29
R_X, Å[d]	0.9	1.04	0.94			1.00	0.89		
ΔE_{ion} , eV [e]	–	–	3.5	18.0	35.0	–	6.2	11.2	25.0

[a] Results of the two-component DFT PBE0 calculations of the cluster models. The YPO_4 column coressponds to the xenotime cluster model Y – $(PO_4)_6$-Y'_{22}-O'_{104}, TPO and UPO correspond to the X – $(PO_4)_6$-Y'_{22}-O'_{104}, X = Th, U clusters, columns $(XPO)^{+n}$, $n = 1,2,3$, X=Th, U correspond to the ionized clusters.
[b] The Bader net charge values of the central atom Q_X (X=Y, Th, U) are obtained with using the computer code [41]. It worth mentioning that the bader charges of Th and U ions with equal formal charges also approximately equal. The equal Thorium ion charge values for the cases of $(TPO)^{+1}$, $(TPO)^{+2}$ and $(TPO)^{+3}$ clusters prove that ionization of the PO_4 group occurs instead of further ionization of the central atom in the former two cases.
[c] The value of total spin for the system, calculated as $\langle|\vec{S}|\rangle = \int \sqrt{S_x(\vec{r})^2 + S_y(\vec{r})^2 + S_z(\vec{r})^2}dV$. For the spin density distribution in the considered clusters, see Fig 3 and Fig 4. The non-zero values of spin of the clusters $(TPO)^{+2}$ and $(TPO)^{+3}$ correspond to the unpaired electrons on the PO_4 groups in these cases.
[d] Lengths of the P – O and X – O bonds. Ionic radii R_X of the Th^{+4} and U^{+4} (see paper [20] and row R_X of this table) are approximately equal to that of the Y^{+3} cation. This statement agrees with that the U^{+4}, Th^{+4} substitutes incapsulated in the crystal deform their nearest environment in much less extent than U^{+3} and Th^{+3} substitutes.
[e] Energy of the cluster ionization $XPO \rightarrow (XPO)^{+n}$, $n = 1,2,3$, X = U, Th calculated as difference between total energies of the corresponding systems.

the cluster with 14 additional electrons, which corresponds to the Th^{+4} oxidation state, the 6*d* shell of thorium is unoccupied. The presence of the spin density peak at 8 a.u. shows that the non-zero total spin value of the clusters with 13 and 12 additional electrons arise from unnatural ionization of the PO_4 groups.

There are experimentally measurable properties of "an atom in a compound" [43] which correlate with oxidation state of a given atom. First of all they are chemical shifts of $K_{\alpha 1}$ and $K_{\alpha 2}$ lines of the x-ray emission spectra (transitions $2p_{3/2} \rightarrow 1s$, $2p_{1/2} \rightarrow 1s$, correspondingly, see [44,45]). We have estimated values of the chemical shifts for the $K_{\alpha 1,2}$ lines in thorium and uranium as yttrium substitutes in xenotime with respect to the corresponding free ion by the method described in papers [43,44]. These data are presented in Table 3. The chemical shifts of the thorium and uranium $K_{\alpha 1}$, $K_{\alpha 2}$ lines are evaluated for the cluster models with 14, 13 and 12 additional electrons in the considered clusters with respect to free U^{4+} and Th^{4+} cations. The chemical shifts of the specific line differ from each other by approximately 100 to 200 meV, for the cases corresponding to different oxidation states of the same impurity cation in xenotime. Difference between $K_{\alpha 1}$, $K_{\alpha 2}$ chemical shifts in the Th-centered clusters with the same oxidation state of thorium is almost zero.

3.4 Frequencies of the localized vibrational modes in the xenotime

Consider frequencies of localized vibrational modes as property of the impurity atoms in xenotime. Such properties for uranium and thorium doped clusters are calculated compared to the cluster with the parent yttrium ion. The vibrational modes in the case of yttrium are, obviously, associated with the vibrational modes of the whole crystal. Thus, one can additionally estimate quality of the given cluster model comparing frequencies of these modes with the results of calculations of xenotime crystal and experi-

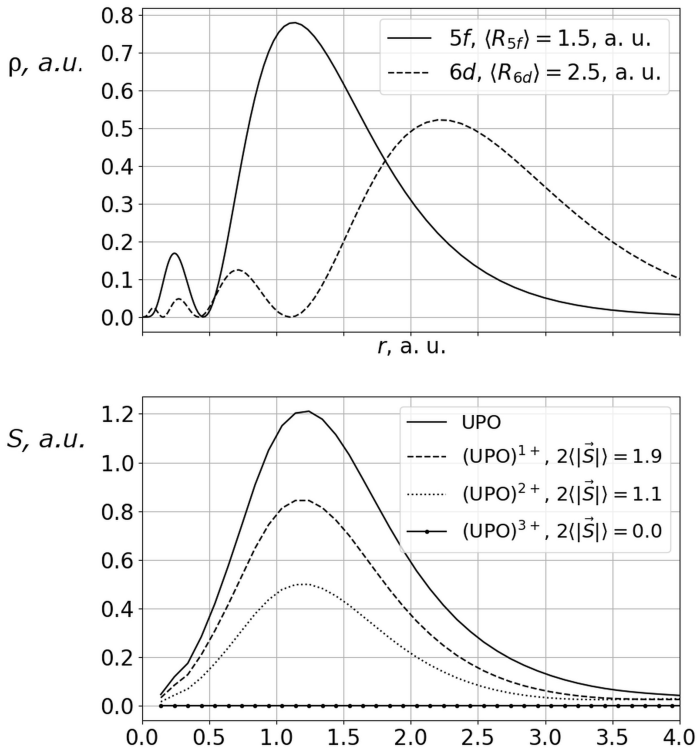

Fig. 3 Radial electron densities corresponding to the $5f$ and $6d$ one-electron states of the uranium neutral free atom calculated with HFD code [46] (at top) and spin density $|\vec{S}(r)| = \sqrt{S_x^2(r) + S_y^2(r) + S_z^2(r)}$ distribution as function of the distance from central uranium atom in the $U-(PO_4)_6 - Y'_{22} - O'_{104}$ clusters (at bottom). The spin density distributions of the clusters with 15, 14, 13 and 12 additional electrons (denoted as UPO , $(UPO)^{+1}$, $(UPO)^{+2}$ and $(UPO)^{+3}$, correspondingly) is almost proportional to each other.

View Article Online
DOI: 10.1039/D0CP02277B

Table 3 Uranium and Thorium x-ray emission spectra $K_{\alpha 1}$ and $K_{\alpha 2}$ lines chemical shifts in xenotime cluster calculations

	U^{4+} [a]	U^{3+}	UPO [b]	$(UPO)^{+1}$	$(UPO)^{+2}$	$(UPO)^{+3}$
$\chi_{2p1/2\to1s1/2}$, meV [c]	0	259	189	-10	-174	-285
$\chi_{2p3/2\to1s1/2}$, meV [c]	0	332	240	-15	-227	-372
	Th^{4+} [a]	Th^{3+}	TPO [b]	$(TPO)^{+1}$	$(TPO)^{+2}$	$(TPO)^{+3}$
$\chi_{2p1/2\to1s1/2}$, meV [c]	0	265	78	7	5	4
$\chi_{2p3/2\to1s1/2}$, meV [c]	0	338	101	10	9	7

[a] Free U^{3+}, U^{4+}, Th^{3+}, Th^{4+} ions with the electronic configurations calculated using the two-component DFT PBE0 framework.

[b] Cluster model calculations of Uranium and Thorium atoms in xenotime (see the Table 2 and the text of the paper for details.)

[c] The chemical shifts values of the energies of Uranium and Thorium $K_{\alpha 1}$, $K_{\alpha 2}$ transitions in xenotime with respect to the corresponding X^{4+} free ion are obtained from the results of electronic structure calculations by the method described in works [43,44].

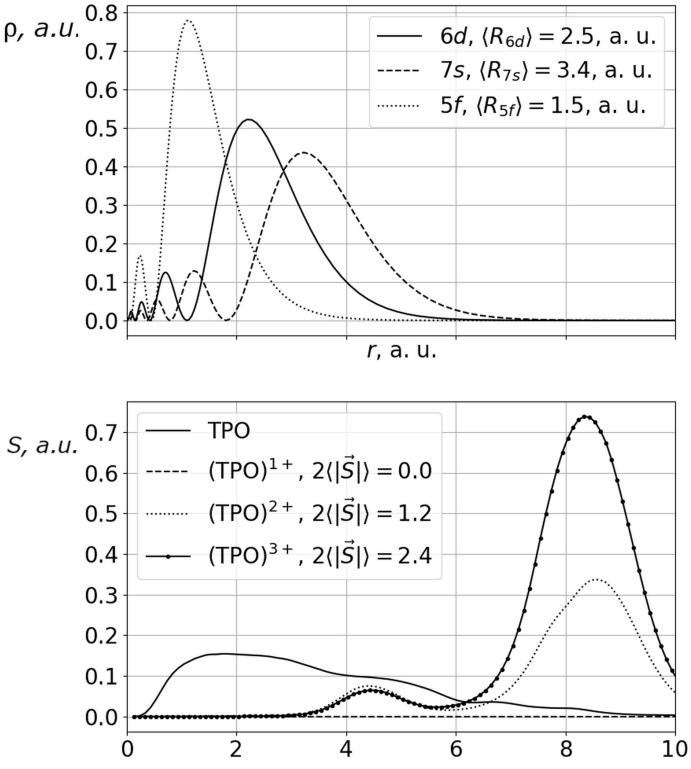

Fig. 4 Radial electron densities corresponding to the $6d$ and $7s$ one-electron states of the free thorium ion with electronic configuration $[Rn]7s^{0.3}7p^{0.3}6d^{0.3}5f^{0.1}$ calculated with HFD code [46] (at top) and spin density $|\vec{S}(r)| = \sqrt{S_x^2(r)+S_y^2(r)+S_z^2(r)}$ distribution as function of the distance from central thorium atom in the $Th-(PO_4)_6-Y'_{22}-O'_{104}$ clusters (at bottom). The spin density distributions of the clusters with 15, 14, 13 and 12 additional electrons (denoted as TPO , $(TPO)^{+1}$, $(TPO)^{+2}$ and $(TPO)^{+3}$ correspondingly) are presented.

mental data. These values are listed in table 4.

Analysis of the frequencies is complicated due to different symmetries of the used cluster model and crystalline structure. The cluster symmetry lowering, mentioned above, leads to many-to-one correspondence between frequencies obtained from the cluster and crystalline calculations. As it follows from our cluster calculations with CTEP modeling the crystal environment, the absolute errors in the vibrational frequencies are within 50 cm^{-1} by the order of magnitude compared to the cristalline study and experimental data.

Table 4 Vibrational frequencies in the xenotime, cm^{-1}

	crystal calculations[a]	cluster model calculations[b]	expt[c]
B_{1g}	189	178 ± 3	185
E_g	200	199 ± 3	210
A_{2g}	217	211	–
E_u	223	228	230
B_{2g}	293	253 ± 20	331
E_g	296	299	299
A_{2u}	320	319 ± 5	307
B_{1g}	326	319 ± 5	316
E_u	346	337	325
A_{1u}	390	362 ± 2	–
A_{1g}	487	484 ± 4	485
E_u	488	508 ± 6	523
B_{2u}	553	530 ± 5	–
E_g	558	549 ± 5	581
A_{2u}	631	652 ± 6	637
B_{1g}	656		659
B_{2u}	978		973
A_{1g}	992	964 ± 10	1001
E_u	1004	1015	997
E_g	1034	1039 ± 7	1026
B_{1g}	1084	1057 ± 2	1058
A_{2u}	1085	1091 ± 5	1059

[a] YPO_4 crystal structure DFT calculations were performed with using CRYSTAL computer code with the PBE0 exchange-correlation functional.

[b] Cluster model calculations data. Frequencies are estimated as eigenvalues of the mass-weighted Hessian calculated for the optimal cluster geometry. Every frequency value obtained from the crystalline structure calculations corresponds to the group of the cluster model frequencies. In this column average frequencies and deviations from them are listed for each group.

[c] Experimental data provided from papers on the Raman and IR spectroscopy analysis of xenotime crystal [47–49].

View Article Online
DOI: 10.1039/D0CP02277B

The frequencies of normal localized vibrational modes for the clusters with the U and Th substitutes of central Y atom are computed and presented in Table 5 along with the results of calculations of normal modes in the xenotime cluster model discussed above. These values depend, obviously, both on chemistry of the central atom and features of its environment and one can note that most of localized modes are associated with interaction of orthophosphate groups with NCE layer in the cluster model. The frequencies of these modes are almost the same for all considered clusters and we did not include them to the table.

Although the results obtained for all cluster models almost coincide, one can see that the frequencies greater than 1000 cm^{-1}, which correspond to the normal modes of the orthophosphate groups near central atom depend first on its oxidation state – frequencies of normal modes in the clusters with the Y^{+3}, U^{+3} and Th^{+3} central ions differ much less from each other than from those in the clusters with U^{+4} and Th^{+4} ions.

Table 5 Frequencies of localized vibrational modes for the Uranium and Thorium impurity ions in the xenotime, cm^{-1}

YPO[a]	UPO	TPO	$(UPO)^{+1}$	$(TPO)^{+1}$
228[b]	213	190	226	227
236	220	208	234	232
275	257	250	277	272
280	264	276	295	291
299	279	280	307	297
299	288	288	317	304
480	446	447	480	477
643	599	612	633	632
958	898	931	962	949
1017	995	1000	987	981
1017	1019	1024	987	986
1034	1034	1030	1005	997
1034	1036	1033	1012	1003
1036	1037	1040	1012	1008
1104	1103	1107	1134	1132
1123	1131	1125	1161	1149
1123	1131	1143	1161	1155
1133	1141	1147	1167	1170

[a] The YPO stands for the neutral xenotime cluster model (with the Y^{+3} ion in center of the cluster), The TPO and UPO stand for cluster with Th^{+3} and U^{+3} impurity ions correspondingly. The clusters with the Th^{+4} and U^{+4} ions are denoted as $(TPO)^{+1}$ and $(UPO)^{+1}$ correspondingly.
[b] Frequencies were estimated as eigenvalues of the mass-weighted Hessian calculated for the optimal cluster geometry.

4 Discussion

The obtained result about energetically most profitable oxidation state uranium(III) (to avoid misleadings arabian designation of both ionic and oxidation states for U and Th, we use below only roman designations for their oxidation states) is in somewhat contradiction with only observed oxidation state U(IV)[5]. Our calculations show that substitution of U(III) instead of Y(III) does not lead to local geometry compression of the U-neighboring orthophosphate groups; they are rather shifted and rotated as a whole (xenotime-to-monazite like structure transformation) with respect to the central atom. Authors of[5] explained absence of the data on existence of U(III) in the crystal by too reducing conditions to form trivalent U in xenotime (see "Introduction"). However, an open question is why the trivalent uranium was also not found in single-atom point defects in natural xenotime, i.e. after geologic-scale storage time?

Our calculations show (see Table 2) that ionization of an electron in the U(III)–$(PO_4)_6$ fragment leads (after its relaxation) to its $[U(IV)–(PO_4)_6]^+$ state (note, that ionizing radiation is inherent to actinide-containing minerals). In turn, electron attachment (EA) to the orthophosphate groups in $[U(IV)–(PO_4)_6]^+$ can hardly be suggested as expected (LUMO energy for orthophosphate group is positive) and only direct EA to vacant $5f$ states of U(IV) is energetically profitable ($5f$-LUMO energy of U(IV) is ≈ -0.2 a. u.) but its ionic radius ($\sim 5f$-orbital size), that is only $\sim$0.1 nm compared to that of whole main cluster, $\sim$0.6 nm, and high angular momentum (l=3) dramatically reduce such a probability. So, we expect that ionization of U(III)-in-xenotime is much more likely than the electron affinity in U(IV)-in-xenotime. Add here that ambient-electron transfer through the orthophosphate barrier from other defects is also unlikely. In turn, ionization of U(IV)-in-xenotime is not profitable compared to the electron affinity to U(V)-in-xenotime since the total Bader charge on neighboring orthophosphate groups, $(PO_4)_6$, is about 1.3 a.u. smaller for U(V)-in-xenotime than that for the case of lowest-energy U(III)-in-xenotime as one can see from Table 2. As a consequence, the $(PO_4)_6$ group around U(V) has a positive electron affinity in our estimates. The detailed radiation analysis of actinide-containing xenotime is not a subject of the present quantum-chemical research, it requires particular consideration elsewhere. The other reason for unobservability of U(III)-in-xenotime is that substitution of neighboring atoms by those with smaller oxidation state takes place in natural xenotime since it may also contain minor Ca(II) on Y site, Si(IV) on P(V) site, F(I) on O site and other elements, which can dramatically change the relative profitability of U(IV) vs. U(III) as is estimated here. Besides, as is noted in Introduction, some more complicated local structures can be more profitable energentcally than solitary U or Th impurities, which can inlcude three neihboring U (Th) atoms as substitutes of Y together with one Y-site vacancy, etc.

5 Conclusions

Results of the embedded cluster calculations of properties of point defects in xenotime containing Th and U atoms are presented and discussed. The electronic structure studies are performed using hybrid DFT functional, PBE0[34], and different versions of the generalized relativistic pseudopotential theory[28]. The cluster model $Y–(PO_4)_6–Y'_{22}–O'_{104}$ for xenotime YPO_4 was used.

The validity of this model is justified by comparing the optimal Y-O and P-O bond lengths obtained from the cluster calculations and corresponding values from the YPO_4 periodic study. Differences between the bond lengths obtained from the cluster model and periodic crystal calculations are of the order of 0.001 Å and are much smaller than differences between results of the crystal structure calculations and experimental data, which are about 0.04 Å. One can conclude that the errors, arising from using the

View Article Online
DOI: 10.1039/D0CP02277B

cluster model are smaller by order of magnitude than those arising from using the PBE0 approximation.

The cluster model calculations of the vibrational frequencies are also carried out. Frequencies obtained in these calculations differ from those obtained in the crystalline calculations and the available experimental data less than 10%

A good agreement of results of cluster modeling and periodic structure calculations for xenotime show that the suggested cluster model with CTEP provides reliable data on the total energy as function of coordinates for the main-cluster atoms. This leads to the possibility of studying embedding of uranium and thorium atoms into the crystal in the framework of the suggested cluster model.

The optimized atomic positions and vibrational frequencies in the cluster study with CTEP are almost equal to those, obtained from periodic structure calculations. Thus, one can conclude that first and second derivatives of total energy with respect to the atomic coordinates are also close.

Using suggested cluster model, the properties of X = U, Th in xenotime were calculated. It has been shown that the oxidation states X(III) are energetically more favorable than X(IV) for the solitary U and Th impurities ($\Delta E \approx 5$ eV).

The x-ray emission spectra chemical shifts of $K_{\alpha 1}$, $K_{\alpha 2}$ lines of Th and U in xenotime compared to the free Th^{4+}, U^{4+} ions were calculated within the cluster models corresponding to the U(III), U(IV), U(V), U(VI) as well as Th(III) and Th(IV) oxidation states of the actinide cations in xenotime. The chemical shift values correlate with the formal charge of the cations, Bader net charges and spin density cluster distributions. Both Th–$(PO_4)_6$–Y'_{22}–O'_{104} cluster models with 13 and 12 additional electrons describe Th(IV) oxidation state in different environments, accordingly; the thorium $K_{\alpha 1}$ and $K_{\alpha 2}$ lines chemical shifts in these cluster models almost equal to each other.

The present calculations of xenotime with solitary Th and U impurities are pilot ones for materials containing actinides within the CTEP approach. Our coming next studies will include several f elements in a local defect of tantalum-niobate minerals (on the example of fersmite crystal with basic formula $Ca(Nb,Ta)_2O_6$) and the structures containing periodically arranged lanthanide atoms, which can have open 4f shell, on examples of YbF_2 and YbF_3 crystals (the latter development of CTEP can also be considered in context of studing line and planar defects in minerals). The further systems of our interest include magnetic materials, crystals and matrices with localized excitations. The phenomena which are planned to be studies using CTEP method include intrinsic localized modes[25] and molecular rotors[24], electronic transitions and magneto-optical effects in point defects[26]. One of attractive perspectives of the CTEP method is in reliable studying those properties of ferroelectrics which cannot be measured but required for interpretation of experiments on search for a "new physics" in the materials (see[27] and refs.).

Conflicts of interest

There are no conflicts to declare.

Acknowledgements

Calculations in the paper were carried out using resources of the collective usage centre "Modeling and predicting properties of materials" at NRC "Kurchatov Institute" - PNPI. We are grateful to Prof. C. van Wullen for the code of modeling the electronic structure with the use of two-component DFT version[36] and to Demidov Yu. A. for the provided yttrium basis set. The work on the GRECP generation for the light elements was supported by the personal scientific fellowship of N.S. Mosyagin of the governor of the Leningrad district. All the other studies were supported by the Russian Science Foundation (Grant No. 20-13-00225).

Notes and references

1 L. Nasdala, S. Akhmadaliev, A. Artac, C. Chanmuang N., G. Habler and C. Lenz, Physics and Chemistry of Minerals, 2018, **45**, 855–871.
2 N. Dacheux, N. Clavier, A.-C. Robisson, O. Terra, F. Audubert, J.-E. Lartigue and C. Guy, Comptes Rendus Chimie, 2004, **7**, 1141–1152.
3 Y. Ji, G. Beridze, D. Bosbach and P. M. Kowalski, Journal of Nuclear Materials, 2017, **494**, 172 – 181.
4 K. Popa, M. Cologna, L. Martel, D. Staicu, A. Cambriani, M. Ernstberger, P. E. Raison and J. Somers, Journal of the European Ceramic Society, 2016, **36**, 4115 – 4121.
5 E. R. Vance, Y. Zhang, T. McLeod and J. Davis, Journal of Nuclear Materials, 2011, **409**, 221–224.
6 Y. Arinicheva, K. Popa, A. C. Scheinost, A. Rossberg, O. Dieste-Blanco, P. Raison, A. Cambriani, J. Somers, D. Bosbach and S. Neumeier, Journal of Nuclear Materials, 2017, **493**, 404 – 411.
7 Z. Yingjie and E. R. Vance, Journal of Nuclear Materials, 2008, **375**, 311–314.
8 E. V. Puchkova, R. V. Bogdanov and R. GierÃľ, American Mineralogist, 2016, **101**, 1884–1891.
9 G. Lumpkin and T. Geisler-Wierwille, Comprehensive Nuclear Materials, Elsevier, Oxford, 2012, pp. 563 – 600.
10 A. Kovács, R. J. M. Konings, J. K. Gibson, I. Infante and L. Gagliardi, Chemical Reviews, 2015, **115**, 1725–1759.
11 A. V. Zaitsevskii, L. V. Skripnikov and A. V. Titov, Mendeleev Communications, 2016, **26**, 307 – 308.
12 A. Kovács, The Journal of Physical Chemistry A, 2017, **121**, 2523–2530.
13 A. Nowak, P. Tecmer and K. Boguslawski, Phys. Chem. Chem. Phys., 2019, **21**, 19039–19053.
14 L. Gyevi-Nagy, M. Kallay and P. R. Nagy, Journal of Chemical Theory and Computation, 2020, **16**, 366–384.
15 A. V. Oleynichenko, A. Zaitsevskii and E. Eliav, arXiv:2004.03682, 2020, 1–6.
16 I. Y. Zhang and A. GrÃijneis, Frontiers in Materials, 2019, **6**, 123.
17 I. V. Abarenkov and M. A. Boyko, Int. J. Quantum Chem., 2016, **116**, 211âĂŞ236.
18 A. L. Tchougréeff, Hybrid Methods of Molecular Modeling, Springer, 2008.

View Article Online
DOI: 10.1039/D0CP02277B

19 S. Höfener, A. Severo Pereira Gomes and L. Visscher, J. Chem. Phys., 2012, **136**, 044104.
20 L. T. Bugaenko, S. M. Ryabyh and A. L. Bugaenko, Vestnik Moscovskogo universiteta, seriya "khimiya", 2008, **49**, 363–384.
21 D. A. Maltsev, Y. V. Lomachuk, V. M. Shakhova, N. S. Mosyagin, L. V. Skripnikov and A. V. Titov, arXiv:1907.06947, 2019, 1–7.
22 V. M. Shakhova, Y. V. Lomachuk, D. A. Maltsev, N. S. Mosyagin, L. V. Skripnikov and A. V. Titov, arXiv:1911.04332, 2019, 1–5.
23 V. M. Goldschmidt, Geochemistry, Oxford, Clarendon Press, 1954, p. 730.
24 A. Comotti, S. Bracco and P. Sozzani, Accounts of Chemical Research, 2016, **49**, 1701–1710.
25 S. V. Dmitriev, E. A. Korznikova, Y. A. Baimova and M. G. Velarde, Physics-Uspekhi, 2016, **59**, 446–461.
26 A. Wickenbrock, H. Zheng, L. Bougas, N. Leefer, S. Afach, A. Jarmola, V. M. Acosta and D. Budker, Applied Physics Letters, 2016, **109**, 053505.
27 L. V. Skripnikov and A. V. Titov, J. Chem. Phys., 2016, **145**,.
28 A. V. Titov and N. S. Mosyagin, Int. J. Quantum Chem., 1999, **71**, 359–401.
29 A. V. Titov and N. S. Mosyagin, Structural Chem., 1995, **6**, 317–321.
30 A. Zaitsevskii and A. V. Titov, Int. J. Quantum Chem., 2013, **113**, 1772–1774.
31 C. Van Wüllen, J. Comput. Chem., 2002, **23**, 779–785.
32 L. V. Skripnikov and A. V. Titov, J. Chem. Phys., 2015, **142**, –.
33 L. F. Pašteka, E. Eliav, A. Borschevsky, U. Kaldor and P. Schwerdtfeger, Phys. Rev. Lett., 2017, **118**, 023002.
34 C. Adamo and V. Barone, J. Chem. Phys., 1999, **110**, 6158–6170.
35 R. Dovesi, A. Erba, R. Orlando, C. M. Zicovich-Wilson, B. Civalleri, L. Maschio, M. RÃľrat, S. Casassa, J. Baima, S. Salustro and B. Kirtman, Wiley Interdisciplinary Reviews: Computational Molecular Science, 2018, **8**, 1360.
36 C. van Wüllen, Z. Phys. Chem., 2010, **224**, 413–426.
37 URL: http://www.qchem.pnpi.spb.ru/Basis, Basis sets for generalized RECPs.
38 M. F. Peintinger, D. V. Oliveira and T. Bredow, Journal of Computational Chemistry, 2013, **34**, 451–459.
39 Y. Ni, J. M. Hughes and A. N. Mariano, American Mineralogist, 1995, **80**, 21–26.
40 Y. Minenkov and L. Cavallo, ACS Omega, 2017, **2**, 8373–8387.
41 W. Tang, E. Sanville and G. Henkelman, J. Phys.: Condensed Matter, 2009, **21**, 084204.
42 R. F. W. Bader, Encyclopedia of Computational Chemistry, Wiley, Chichester, U.K., 1998, vol. 1, pp. 64–86.
43 A. V. Titov, Y. V. Lomachuk and L. V. Skripnikov, Phys. Rev. A, 2014, **90**, 052522.
44 Y. V. Lomachuk and A. V. Titov, Phys. Rev. A, 2013, **88**, 062511.
45 Y. V. Lomachuk, Y. A. Demidov, L. V. Skripnikov, A. V. Zaitsevskii, S. G. Semenov, N. S. Mosyagin and A. V. Titov, Optics and Spectroscopy, 2018, **124**, 472–477.
46 I. I. Tupitsyn, G. B. Deyneka and V. F. Bratzev, HFD, a program for atomic finite-difference four-component Dirac-Hartree-Fock calculations on the base of the HFD code[?] .
47 M. Giarola, A. Sanson, A. Rahman, G. Mariotto, M. Bettinelli, A. Speghini and E. Cazzanelli, Phys. Rev. B, 2011, **83**, 224302.
48 A. N. Lazarev, A. N. Mazhenov and A. P. Mirgorodskii, Izv. Akad. Nauk SSSR, Neorg. Mater., 1978, **14**, 2107.
49 A. Armbruster, Journal of Physics and Chemistry of Solids, 1976, **37**, 321 – 327.